Available online at www.sciencedirect.com
SCIENCE DIRECT
International Journal of Heat and Mass Transfer 49 (2006) 3313–3324
International Journal of HEAT and MASS TRANSFER
www.elsevier.com/locate/ijhmt

Forced convection in metallic honeycomb structures

T. Wen [a], J. Tian [a], T.J. Lu [a,b,*], D.T. Queheillalt [c], H.N.G. Wadley [c]

[a] *Engineering Department, Cambridge University, Cambridge CB2 1PZ, UK*
[b] *School of Aerospace, Xian Jiaotong University, Xian 710049, PR China*
[c] *Materials Science Department, University of Virginia, Charlottesville VA 22904-4745, USA*

Received 20 October 2005
Available online 24 May 2006

Abstract

The heat transfer and pressure drop characteristics of sandwiched metallic honeycomb structures, with one face-sheet heated by constant heat flux and cooled by forced air convection, have been investigated both experimentally and numerically. Six test samples, made of two materials with different thermal conductivities (16.2 W/(mK) for stainless steel and 401 W/(mK) for pure copper), were evaluated. The effect of cell shapes was also explored using samples with square, diamond, trapezoidal and hexagonal shapes. Good agreements between experimental and numerical results were obtained for both the friction factor (pressure drop) and heat transfer rate. The results show that the overall pressure drop is correlated with surface area density and cell shape, whereas the overall heat transfer rate is a function of surface area density, cell shape, the ratio t/H, and the thermal conductivity of the solid material. Comparisons with other heat sink media have also been made. They indicate that the metallic honeycomb structures investigated are excellent candidates for heat sink applications.

Keywords: Forced convection; Metallic honeycomb structures; Experiment; Numerical calculation

1. Introduction

There are two broad classes of cellular materials, one with a stochastic topology (foams) and the other with a periodic structure (lattice truss structures, prismatic structures, etc.) [1]. Whilst stochastic metal foams with open cells have attractive thermal, acoustic and energy absorption properties [2–4], their load bearing capability is significantly inferior to periodic structures having the same weight due to different deformation mechanisms (bending versus stretching) [5]. The efficient load support afforded by periodic structures has led to an interest in the use as multifunctional materials having multiple roles such as structural load support, thermal management, impact energy absorption, sound absorption, actuation, energy storage, and so on. They appear most attractive for applications where the cellular structures are used as the core of sandwich panels/shells where they promise lower weight than competing materials and structural concepts [1]. Potential applications include actively cooled supersonic aircraft or spacecraft skins, acoustic liners and cooling jackets for combustors and jet engines, and lightweight structural elements with sensing and actuation capabilities [6–10].

Prismatic structures with a single "easy flow" direction appear particularly interesting for heat sink applications. Among all these structures, the potential of metallic honeycomb structures as compact heat sinks has recently drawn significant attention. Using a modified fin analogy model, Lu [11] evaluated the performance of metallic honeycombs with hexagonal cells subjected to forced convection. Gu et al. [12] extended the approach and developed analytical models and dimensionless indices that enable simultaneous evaluation of the structural and heat transfer performance of metallic honeycomb structures with square, triangular and hexagonal cells. A two-stage optimization was carried out to identify cell morphologies that optimize the

* Corresponding author.
E-mail address: tjlu@mail.xjtu.edu.cn (T.J. Lu).

0017-9310/$ - see front matter © 2006 Elsevier Ltd. All rights reserved.
doi:10.1016/j.ijheatmasstransfer.2006.03.024

Nomenclature

B	shape number [–]
c_p	specific heat at constant pressure [kJ/(kgK)]
D_h	hydraulic diameter [m]
f_H	friction factor based on overall height of sample [–]
$f_{H,f}$	friction factor based on overall height of sample due to frictional pressure drop [–]
$f_{H,l}$	friction factor based on overall height of sample due to local pressure drop (inlet and outlet) [–]
Gr	Grashof number [–]
$\bar{h}$	overall heat transfer coefficient [W/(m^{2}K)]
$h(z)$	local heat transfer coefficient [W/(m^{2}K)]
H	overall height of sample (excluding thickness of face-sheets) [m]
j_H	Colburn factor based on overall height of sample [–]
k	thermal conductivity [W/(mK)]
l, l_{bottom}, l_{up}	cell sizes (shown in Fig. 1) [m]
L	overall length of sample [m]
N	number of local measurement along axial direction [–]
Nu_H	Nusselt number based on overall height of sample [–]
P	pumping power [W]
ΔP	pressure drop [Pascal]
ΔP_f	frictional pressure drop [Pascal]
ΔP_l	local pressure drop [Pascal]
Pr	Prandtl number [–]
q	heat flux [W/m^2]
Q	total heat input [W]
Re_{d_h}	Reynolds number based on cell size [–]
Re_H	Reynolds number based on overall height of sample [–]
t	cell wall thickness [m]
T	temperature [K]
$T(z)$	local temperature [K]
U	mean velocity in cells [m/s]
U_m	mean air velocity upstream of sample [m/s]
W	overall width of sample [m]
x, y, z	Cartesian coordinate (shown in Fig. 1) [–]

Greek symbols

β	Coefficient of thermal expansion [K^{-1}]
ε	porosity [–]
ϕ	surface area density [1/m]
μ	dynamic viscosity [kg/(ms)]
ν	kinematic viscosity [m^2/s]
Π_h, Π_P	two dimensionless indices characterizing the overall heat transfer rate and overall mechanical pumping power for different heat sinks [–]
θ	angle (shown in Fig. 1) [degree]
ρ	density [kg/m^3]
$\tilde{\rho}$	relative density [–]

Subscripts

f	fluid
in	inlet
max	maximum
out	outlet
s	solid
w	wall

structural and heat transfer performance for a specified relative density. In addition to these theoretical analyses, Kumar and McDowell [13] used a finite element method to analyse steady-state convective heat transfer through honeycomb structures with rectangular cells and explored optimized functionally graded honeycomb structures. Using the finite difference method for steady-state heat transfer and a multi-objective decision support model, Seepersad et al. [14] designed both periodic and functionally graded honeycomb structures with desirable structural and thermal capabilities.

Experimental studies of convective heat transfer in extruded metallic honeycomb structures have been performed by Hayes et al. [15] and by Dempsey et al. [16]. However, a systematic study on the topology and the role of solid thermal conductivity has not yet been reported. Additional experimental data are therefore needed to validate analytical and numerical models. Here, six different metallic honeycomb structures, made of two different materials with thermal conductivities of 16.2 W/(mK) (stainless steel) and 401 W/(mK) (pure copper), were fabricated (see Section 2). Steady-state convective heat transfer experiments were then carried out on sandwich structures made from these cores with a uniform heat flux applied on one face-sheet and thermal insulation imposed on the other (see Section 3). The commercial CFD (computational fluid dynamics) code FLUENT was used to predict the steady-state heat transfer performance of metallic honeycomb structures (see Section 4). The experimental results are compared with the CFD predictions for validation; and the comparisons of the heat transfer performance between six test samples, and also between these test samples and other lightweight heat sink media, including open-celled metal foams, lattice framed structures and brazed woven textile lattices are given (see Section 5).

2. Test samples

2.1. Fabrication procedure for stainless steel samples

The four stainless steel samples are shown in Figs. 1(a)–(d) and their corresponding periodic unit representatives

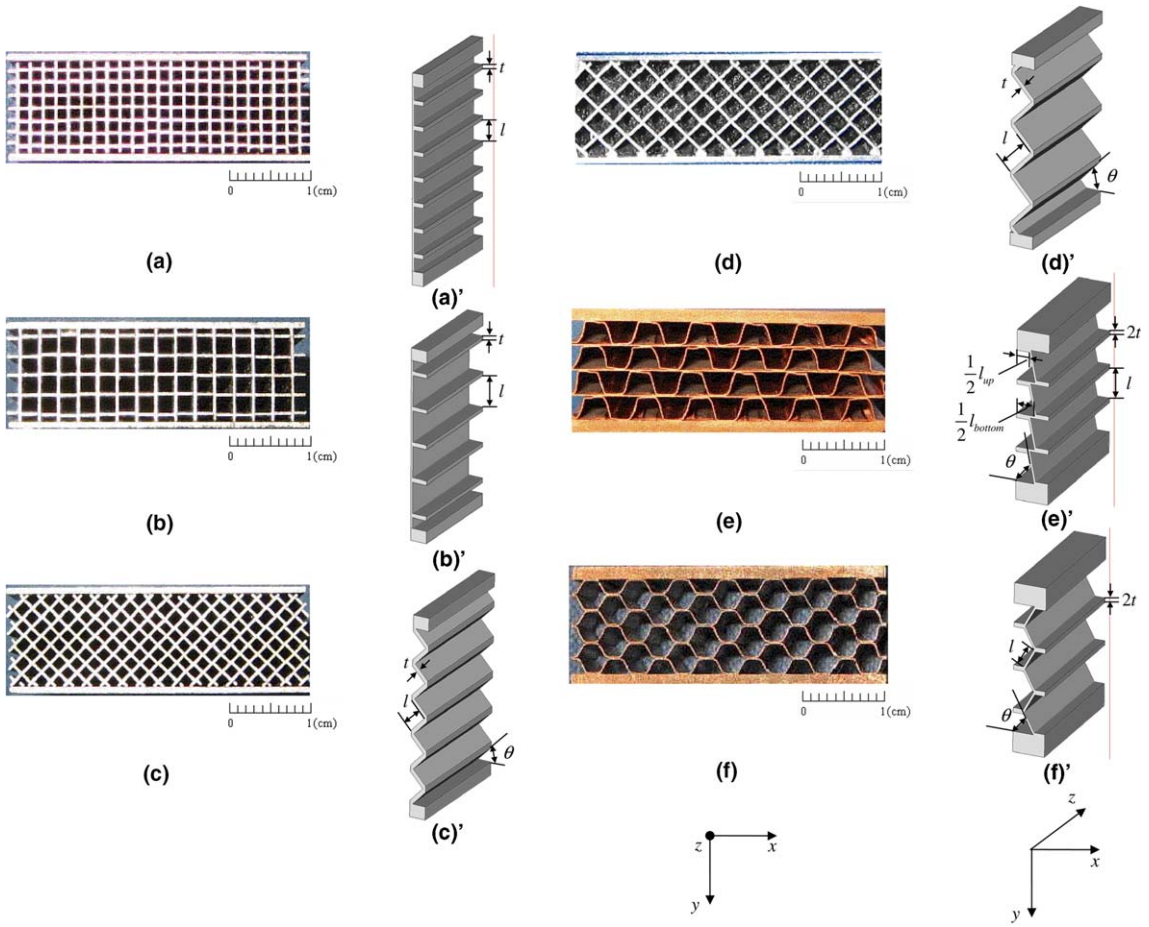

Fig. 1. Photos of six test samples and their corresponding computational domains for numerical calculations.

are shown in Figs. 1(a)′–(d)′. To fabricate the sample, individual stainless steel sheets (density $\rho_s = 8000$ kg/m^3, solid thermal conductivity $k_s = 16.2$ W/(mK)) were first cut into pieces, with the length of the through-thickness slots equal to half the sheet width. The sheets were then assembled according to the desirable topology, as illustrated in Fig. 2(a). The assembly was sprayed with a mixture of polymer-based cement (Nicrobraz® Cement 650) and Ni–25Cr–10P brazing alloy powder (Nicrobraz® 51). The solidus and liquidus of this alloy are 880 and 950 °C whereas the melting point of stainless steel is over 1300 °C. To construct a sandwich, two 0.9 mm thick stainless steel face-sheets sprayed with the same mixture were attached to the assembly (note that rotating square cores 45° about

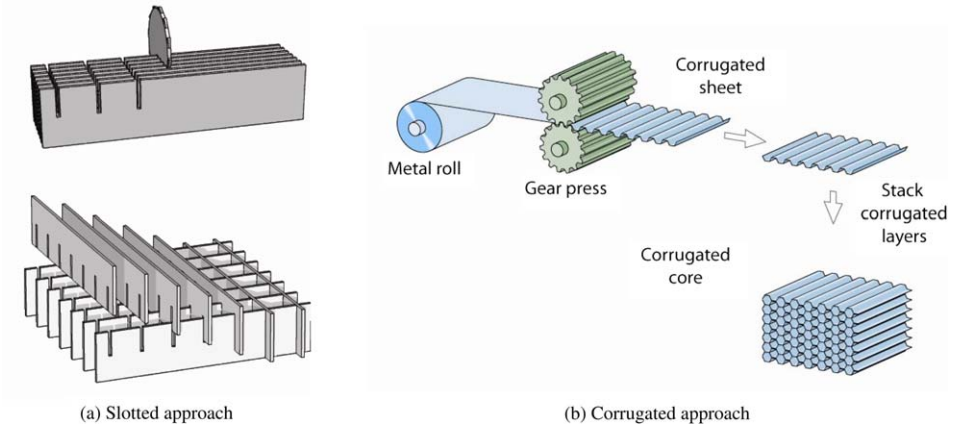

Fig. 2. Illustration of sample assembling.

Table 1
Design parameters for test samples

#	Material	Cell shape	t (mm)	l (mm)	l_{bottom} (mm)	l_{up} (mm)	θ (°)	L (mm)	W (mm)	H (mm)	ε	ϕ (1/m)
1	Stainless steel	Square	0.3	1.4	–	–	–	50	40	12	0.6782	1937.7
2	Stainless steel	Square	0.3	2.3	–	–	–	50	40	12	0.7825	1360.9
3	Stainless steel	Diamond	0.3	1.4	–	–	45	50	40	12	0.6782	1937.7
4	Stainless steel	Diamond	0.3	2.3	–	–	45	50	40	12	0.7825	1360.9
5	Copper	Trapezoid	0.2	2.6	3.5	2.4	78	60	40	12	0.842	1231.8
6	Copper	Hexagon	0.2	2.0	–	–	60	60	40	12	0.860	1125.0

the z-axis results in the formation of the diamond cores). The whole sandwich sample was then heated within flowing argon (at a vacuum level of approximately 10^{-1} Torr), at a rate of 20 °C/min to 550 °C to volatilise the polymer cement. The system was then evacuated to a vacuum level of less than 10^{-3} Torr and the temperature was ramped at a rate of 20 °C/min to 1000 °C and held there for 15 min.

2.2. Fabrication procedure for copper samples

The two copper samples are shown in Figs. 1(e)–(f) and their corresponding periodic unit representatives are shown in Figs. 1(e)′–(f)′. To fabricate the samples, individual copper sheets ($\rho_s = 8960$ kg/m^3, $k_s = 401$ W/(mK)) were first crimped into the designed shape via rolling (Innovent, Peabody, MA). The cores were cut and assembled into the desired topology with copper interlayer sheets and 1.8 mm thick copper face-sheets to create the sandwich panels; see Fig. 2(b). Both the interlayer and face-sheets were coated with a thin layer of CuproBraz® viscous brazing paste. The brazing filler metal, developed for CuproBraz®, belongs to the CuSnNiP-family. This filler metal was OKC600 and has a nominal composition of: Ni-42%, Sn-15.6%, P-5.3%, Cu-balance. The braze coated sandwich assemblies were air dried in a warming oven then transferred to a vacuum furnace and heated under a partial pressure of argon (250 mTorr) at a rate of 30 °C/min to 650 °C and held for 15 min, followed by a rapid furnace cool.

2.3. Sample morphology

For a honeycomb structure with periodically identical cells, its geometry can be uniquely defined by five parameters:

(1) Cell shape (hexagonal, square, etc.).
(2) Stacking order (Gu et al. [12]), which depends mainly on the fabrication method.
(3) Porosity ε, which is defined as the ratio of the void volume to the total volume of the honeycomb structure. In some papers, relative density $\tilde{\rho}$ is used, which is the ratio between the mass of the honeycomb structure and the mass of the base material having the same volume. They are simply related as $\tilde{\rho} = 1 - \varepsilon$.
(4) t/H, which is the ratio between the cell wall thickness and the overall height of the structure (excluding the thickness of two face-sheets).
(5) H/L, which is the ratio of overall height to length of the structure.

The first four parameters determine the cross-sectional topology of the honeycomb structure, and the last one decides its overall dimension. The overall width of the structure, W, is not an important parameter in most situations as its properties in the width direction can be representatively defined by those of a periodic unit.

The surface area density ϕ, which is defined as the total heat transfer area divided by the volume of the structure, is an important parameter when discussing the thermal performance of a structure. For honeycomb structures, it depends on the cross-sectional topology of the structure and therefore is a function of the cell shape, the stacking order, ε and t/H. For specified cell shape and stacking order, the effects of ε and t/H on ϕ are obvious: either increasing t/H with ε unchanged or increasing ε with constant t/H will reduce ϕ. The different stacking orders influence ϕ by overlapping part of the convective heat transfer area and changing them to the interfaces between solid walls.

The detailed parameters for the present test samples are given in Table 1.

3. Experimental measurements

3.1. Experimental apparatus

A schematic diagram of the experimental setup, consisting of three sections: air suction system, test section, and data acquisition system, is depicted in Fig. 3.

Air flow is achieved by a suction located downstream of the test section. The mass flow rate is controlled by a flow regulator valve, located between the exit of the test section and the suction. Before air enters the sample, efforts are made to ensure that the air flow is hydraulically fully developed by adding several additional parts, which include a wire screen layer, a honeycomb layer, and another wire screen layer, followed by a 9:1 contraction and a flow developing channel region (with a length to height ratio of about 35).

A constant heat flux is imposed on the bottom face-sheet of the sample by a heating element (silicone–rubber wire wound, from Watlow Inc.). The heat flux released from the heating element was adjusted by changing the voltage of a power supply, which has an output voltage range 0–

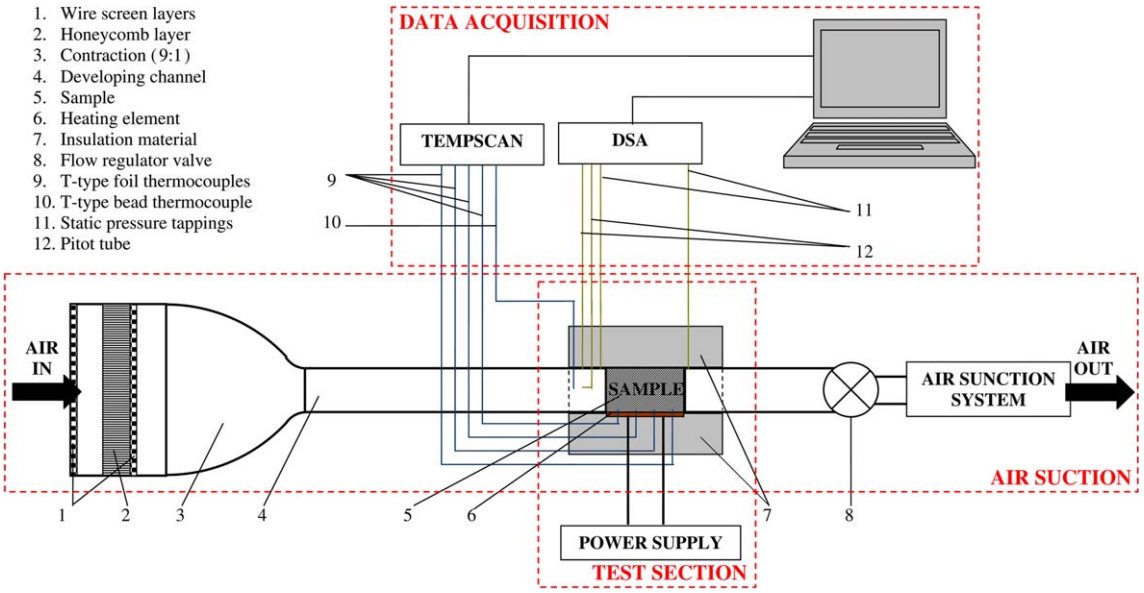

Fig. 3. Schematic of test rig (not proportional to real size).

240 V corresponding to a heat input of 0–32 W. To ensure uniformity of the heat flux, a heat spreader (0.9 mm thickness) made of pure copper is inserted between the bottom face-sheet and the heating element. Four T-type foil thermocouples (from RdF Corp.) are equidistantly mounted along the flow direction between the bottom face-sheet and the heat spreader. The whole sample region is surrounded by insulation materials to minimize heat loss (see Fig. 4). A Pitot tube is positioned before the sample to monitor the mainstream velocity at the inlet of the sample. Given the blockage ratio, i.e. the ratio of channel height (12 mm) to tube outer diameter (0.51 mm), is 23.5, wall interference effect on the Pitot tube is expected to be negligible. Two additional static pressure tappings are located separately at the inlet and outlet of the sample to measure the pressure drop through the sample. A T-type bead thermocouple is inserted into the channel centre before the entrance of the sample to monitor the air inlet temperature.

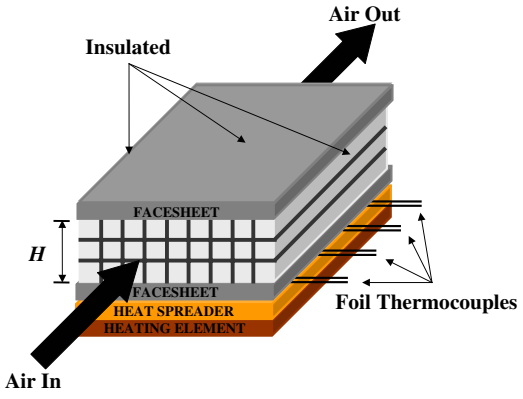

Fig. 4. Schematic diagram of thermal boundary conditions assembly (not proportional to real size).

All the pressure probes are connected to the DSA 3217 (Digital Sensor Arrays, from Scanivalve Corp.), which scans the pressure values and outputs data via Ethernet using TCP/IP protocol to the PC. All the thermocouples are connected to a pre-calibrated temperature scanner TempScan®, which sends data to the PC via RS232 serial port. The data acquisition is under the control of a LabVIEW™ program.

3.2. Experimental procedure

Tests were carried out for six test samples (shown in Fig. 1) at different air mass flow rates and for three hear fluxes: $q = 2000$, 4000 and 8000 W/m^2.

During a typical experimental run, a constant power input was supplied and the air mass flow rate was adjusted by the valve until the pre-specified value was achieved. The inlet velocity, pressure drop, air temperature and four temperatures along the bottom face-sheet of the sample were simultaneously monitored. When the variation of the temperature did not exceed 0.1 °C (within a period of 3 min in general), steady state was assumed to be reached; and a set of data were collected. Then the valve was adjusted to achieve a new air mass flow rate, and the above procedure was repeated.

3.3. Data reduction

The fluid friction and heat transfer rate can be evaluated by the friction factor and the Nusselt number, respectively, which are generally plotted as functions of the Reynolds number. Since the primary goal of the present study is to determine the overall thermal performance of the metallic honeycomb structures with different topologies, the overall height H is used as the length scale, which is also

convenient for the comparison with other heat sink media. Three non-dimensional groups based on the overall height H: Reynolds number Re_H, friction factor f_H and Nusselt number Nu_H are respectively defined as

$$f_H = \left(\frac{\Delta P}{L}\cdot H\right)\cdot\left(\frac{1}{\rho_f U_m^2/2}\right) \tag{1}$$

$$Nu_H = \frac{\bar{h}H}{k_f} \tag{2}$$

$$Re_H = \frac{U_m H \rho_f}{\mu_f} \tag{3}$$

where U_m is the air mean velocity upstream of the test sample measured by the Pitot tube and $\bar{h}$ is the overall heat transfer coefficient, which can be obtained from the spatial average of the local heat transfer coefficient:

$$h(z) = \frac{q}{T_w(z) - T_f(z)} \tag{4}$$

by

$$\bar{h} = \frac{1}{L}\sum_1^N h(z)\Delta z \tag{5}$$

Here, $T_w(z)$ is the measured temperature of the bottom face-sheet of the test sample and the temperature in the air $T_f(z)$ is calculated based on the measured inlet temperature by imposing energy conservation along the axial (z) direction, as:

$$T_f(z) = T_{f,in} + \frac{q}{\rho_f U_m H c_p} z \tag{6}$$

All the air properties are based on the mean fluid temperature $(T_{f,in} + T_{f,out})/2$ and interpolated from the tabulated thermo-physical properties of air.

3.4. Experimental uncertainty

An error analysis following the method described in Coleman and Steele [17] was performed to determine the uncertainty in the experimental data. Since the air properties were interposed from standard tables, their uncertainties are assumed to be negligible. The uncertainty in pressure drop measurement was estimated to be less than 2%. The total heat loss in the present study was estimated less than 5% and the uncertainty in temperature measurement is estimated as 4% including errors from thermocouples and the TEMPSCAN. Therefore, using the root-square method, the uncertainties for the Reynolds number, the friction factor and the Nusselt number were estimated to be less than 1.0%, 2.83% and 6.4%, respectively.

4. Numerical simulations

The commercially available CFD code FLUENT [18] was used to predict the steady state heat transfer performance of metallic honeycomb structures.

4.1. Computational domain

Since the sample is thermally insulated at both ends $x = W/2$ and $x = -W/2$ (see Fig. 4), and the cell size is typically much smaller than the overall width of the sample (the maximum ratio of the cell size to overall width is about 0.08), it is assumed that the thermal and hydraulic fields are independent of the transverse coordinate x. The periodic units shown in Figs. 1(a)′–(f)′ are chosen as the calculation domain. The existence of smaller-sized cells near two face-sheets leads to the different flow distributions in cells along vertical coordinate y, which is considered by introducing a flow developing channel before the sample as that in test rig.

4.2. Grid generation

For the convenience of grid generation, the whole computational domain is divided into a number of regular geometries having different cross-sectional shapes but the same length L. The cross-sectional grids are generated according to the shape of each cross-section, with those near the wall refined. The same disposition is employed at all axial stations. The size of the forward step is varied. The initial step size is chosen to be of the order of one percent of the overall length. It is increased at each subsequent station by a constant factor in the first 20 steps; thereafter the steps are equally distributed.

4.3. Boundary conditions

(1) A velocity-inlet boundary condition with a uniform value was assumed at the entrance of the inlet channel; and a pressure-outlet boundary condition with zero gauge pressure was employed at the exit of the sample cell duct.
(2) A constant heat flux boundary condition was employed at the bottom face-sheet of the sample, while the top and bottom walls of the flow developing channel as well as the top face-sheet of the sample were insulated.
(3) Symmetrical boundary conditions for all side surfaces of the sample in the x-direction (sample's width) were employed.
(4) The inner surfaces of each cell were set as coupled thermal conditions so that the heat exchange between adjacent zones, belonging to the solid region and the fluid region, respectively, can be calculated. In the fluid side of these inner surfaces, non-slip boundary condition was employed.
(5) Since the flow developing channel was included only to calculate the flow distributions in different sized cell ducts, a zero-shear boundary condition was employed at the inner surface of the inlet channel so that the inclusion of the inlet channel does not affect the uniformity of velocity distribution upstream the inlet of the sample.

4.4. Convergence criterion

At the end of each iteration, the maximum changes in the value of each dependent variable are calculated. When the maximum of these changes is reduced to a value below a pre-set convergence criterion, the calculation is deemed converged. In the present calculations, this criterion is set as 1×10^{-7}.

4.5. Grid sensitivity

For each sample, two grids with approximately 200,000 and 1,000,000 cells were generated and the calculation results based on these two grids were compared. The results show that the maximum difference in predictions is within 2% for the two grids, and hence the grid with 200,000 cells is chosen for all the subsequent calculations.

5. Results and discussions

5.1. Comparisons between experimental and numerical results

A laminar flow model was used in the CFD calculations and all the calculations were carried out within $Re_H < 10{,}000$, corresponding to a maximum Reynolds number based on the cell size smaller than 2000.

For convenience of comparing the CFD predicted heat transfer and pressure drop with those measured experimentally, the Colburn factor j_H [19] is used in lieu of Nu_H, which is defined as:

$$j_H = \left[\frac{Nu_H}{Re_H Pr}\right] Pr^{2/3} \tag{7}$$

Fig. 5 compares the predicted friction factor f_H and Colburn factor j_H with those measured for each test sample. As a whole, in the predicted range, the CFD results agree well with the experimental results. For the friction factor f_H, however, the CFD results are slightly steeper than the experimental results. The reason lies in the fact that, in CFD calculations, a uniform velocity distribution is applied at the inlet of the sample; while in the experiment, the non-slip boundary condition on the inner surface of the developing channel makes the velocity distribution upstream of the sample a typical Poiseuille profile. Therefore, the fluid velocity near the two face-sheets, where the smaller-sized cells locate, is higher in the CFD calculation than that in the experiment, which leads to a higher mass flow rate in these smaller-sized cells in prediction and, correspondingly, a lower mass flow rate in the major cells. The increase of pressure loss due to the increase of fluid velocity (or mass flow rate) becomes larger when the cell size becomes smaller ($\Delta P \sim U/D_h^2$). The overestimation of the pressure drop in smaller-sized cells exceeds the underestimation of the pressure drop in major cells. Therefore in low Reynolds number region, where laminar flow prevails, the CFD prediction is slightly higher than the experimental results. However, with increasing Reynolds number, local disturbance of the flow due to structural imperfections at the cell level due to manufacturing may cause additional pressure loss; this effect is not captured by the present laminar CFD model. Furthermore, in high Reynolds number region, this disturbance may turn the laminar flow into turbulent flow, where the friction factor is even higher and its trend is flatter.

The good agreement between CFD predictions and experimental measurements on both the pressure drop and heat transfer rate give confidence to perform further CFD calculations, the results of which are presented below.

5.2. Pressure drop

Fig. 6 plots the experimentally measured friction factor f_H as a function of the Reynolds number Re_H for all the samples. For samples 1 and 3 with cell size ~1.4 mm, the Reynolds number based on the overall height, Re_H, falls in the range of 1000–20,000, corresponding to the range of the Reynolds number based on the cell size, Re_{d_h}, as 120–2300. Consequently, in this regime, laminar flow prevails. It can be seen from Fig. 5 that f_H is inversely proportional to Re_H for these two samples. For samples 2 and 4 with cell size ~2.3 mm, the Re_H range is 2000–30,000, which corresponds to the Re_{d_h} range of 380–5500. In general, the friction factor f_H is inversely proportional to Re_H when $Re_H < 12{,}000$ (corresponding to $Re_{d_h} < 2300$) and then tends to approach an asymptotic value as Re_H is increased, the latter mainly due to the appearance of transition flow or turbulent flow in cells resulting from larger Re_{d_h}. For samples 5 and 6, which have even larger cell sizes, the curves present similar tendency as those of samples 2 and 4, and the Re_H corresponding to the transition of flow occurs at ~10,000.

The pressure drop through honeycomb structures consists of two parts: local pressure loss (inlet and outlet) ΔP_l and frictional pressure loss ΔP_f:

$$\Delta P = \Delta P_l + \Delta P_f \tag{8}$$

Local pressure loss ΔP_l can be calculated from [20]:

$$\Delta P_l = K \frac{\rho_f U_m^2}{2} \tag{9}$$

K is the loss coefficient due to a sudden contraction and a sudden expansion at the inlet and outlet of the sample respectively. It is a function of sample's porosity ε: when ε increases from zero to unit, K decreases continuously from 1.5 to zero [20].

For the non-dimensional friction factor based on the core height, Eq. (8) yields

$$f_H = f_{H,l} + f_{H,f} \tag{10}$$

where

$$f_{H,l} = K \frac{H}{L} \tag{11}$$

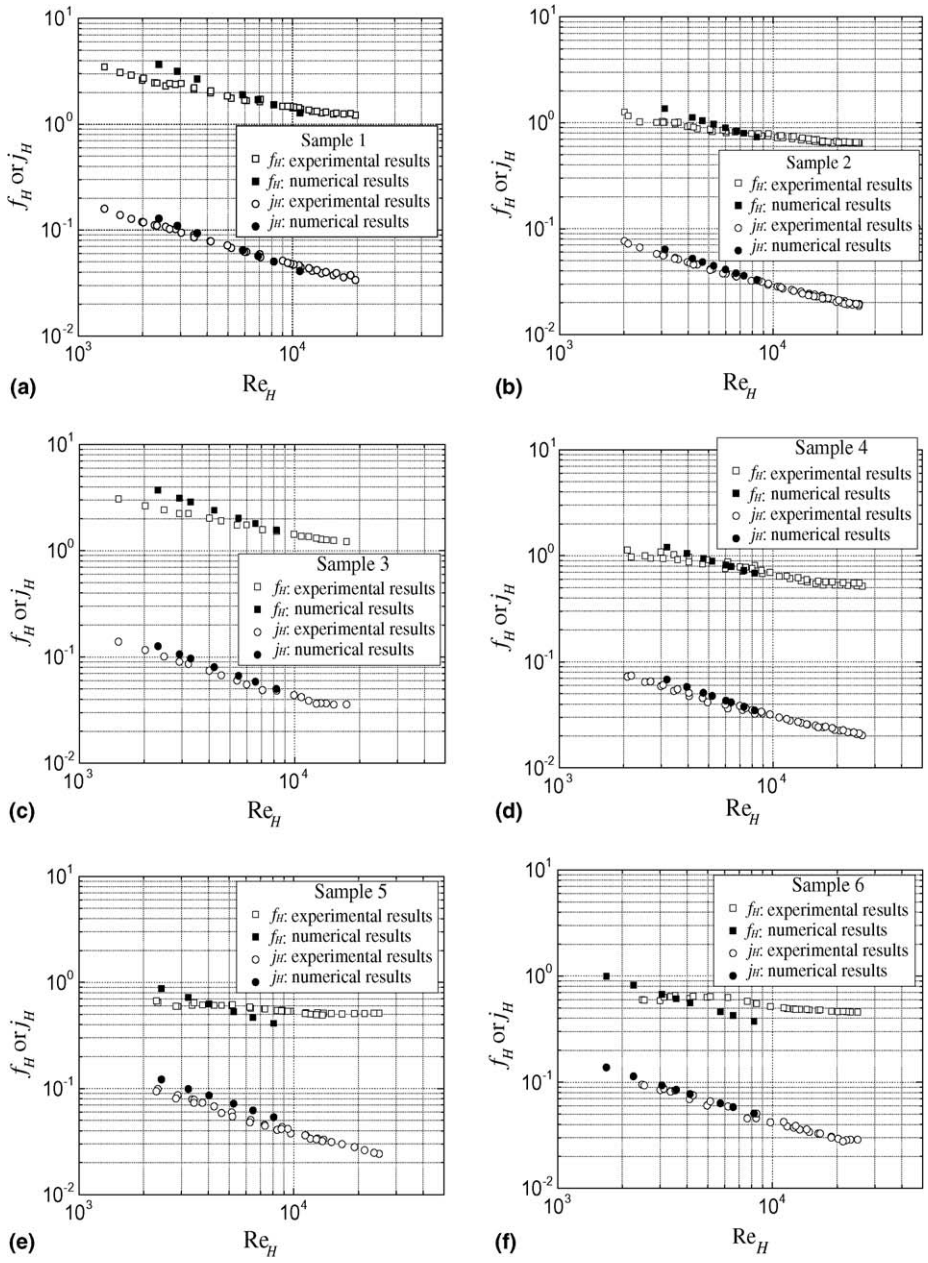

Fig. 5. Comparisons of friction factors f_H and Colburn factors j_H between experimental and numerical results.

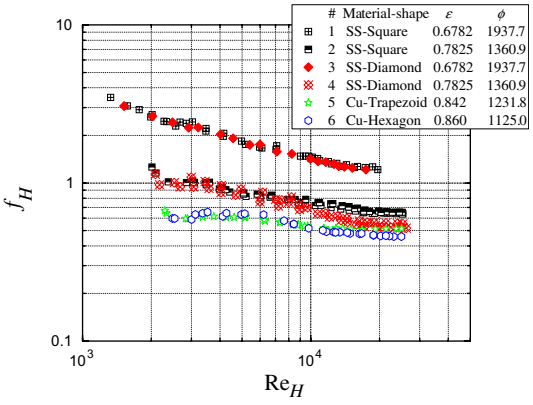

Fig. 6. Friction factors f_H of six test samples plotted as functions of Reynolds number Re_H.

and

$$f_{H,f} = \frac{\Delta P_f}{L} \cdot H \cdot \frac{1}{\rho_f U_m^2/2} \tag{12}$$

Therefore, the friction factor due to the local pressure loss $f_{H,l}$ is only related to the geometric parameters of the sample. Its values for the present six test samples are given in Table 2. For present samples and test ranges, $f_{H,l}$ is comparatively small relative to the overall friction factor f_H ($f_{H,l} < 0.04 f_H$). Moreover, with the increase of the porosity, the percentage of $f_{H,l}$ in f_H becomes even smaller and the effect of the porosity on the friction factor can be ignored. In other words, the pressure drop is mainly due to the frictional pressure loss, ΔP_f, which is mainly related with two factors: *surface area densities* ϕ and *cell shape*.

Table 2
$f_{H,l}$ for test samples

#	ε	K	$f_{H,l}$	f_H	$f_{H,l}/f_H$ (%)
1	0.6782	0.1819	0.04366	1.2162–3.4801	1.25–3.59
2	0.7825	0.08616	0.02068	0.6372–1.2625	1.64–3.25
3	0.6782	0.1819	0.04366	1.2161–3.0665	1.42–3.59
4	0.7825	0.08616	0.02068	0.5180–1.1360	1.82–3.99
5	0.842	0.04652	0.0093	0.4907–0.6675	1.39–1.90
6	0.860	0.03679	0.00736	0.4580–0.6552	1.12–1.60

An obvious relationship between the friction factor f_H and the surface area density ϕ is clearly shown in Fig. 6: for honeycomb structures having the same cell shape, the larger the surface area density, the higher the friction factor. This can be easily understood since higher surface area density means more frictional areas per unit volume, causing more pressure loss.

Before discussing the effect of cell shape, a dimensionless group $B = (\pi D_h^2/4)/A_{duct}$ is introduced, which is initially defined by Bejan [21] as a shape number to explain the different pressure drop and heat transfer behavior in two-dimensional ducts having different cross-sectional shapes. D_h and A_{duct} represent, respectively, the hydraulic diameter and the area of the shape. For hexagonal, square (diamond), and trapezoidal cell shapes in the present samples, $B = 0.907$, 0.785, and 0.765, respectively. Generally speaking, the larger the shape number B is, the higher the friction and heat transfer rate are [21].

In Fig. 6, for honeycomb structures with square and diamond cells having the same porosity and surface area density (sample 1 vs. sample 3, sample 2 vs. sample 4), their cell shapes are actually identical except for the cross-sectional direction. For air flow, this directional difference leads to negligible differences in the flow field since the force effects in cross section (gravity, buoyancy, etc.) can be ignored relative to the viscous forces (the Grashof number, $Gr = g\beta\Delta TV/v^2$, which denotes the ratio of the buoyancy force to viscous force, has a value of 10^{-5}). Therefore, it is not surprising that samples 1 and 2 (square cells) have nearly the same friction factor curves as those of samples 3 and 4 (diamond cells), respectively. For trapezoid-shaped sample 5 and hexagon-shaped sample 6, despite their different surface area densities, their friction factors are nearly the same. The reason is that the larger shape number of the hexagon-shaped sample 6 compensates for its smaller surface area density.

5.3. Heat transfer

Fig. 7 depicts the Nusselt number Nu_H as a function of Reynolds number Re_H. Besides the experimental data for six test samples, another two sets of data obtained from CFD calculations for geometries identical with samples 3 and 4 but with solid material replaced by copper ($\rho_s = 8960$ kg/m^3, $k_s = 401$ W/(mK)) were supplemented. As a whole, Nu_H for all the samples increases with the increase of Re_H.

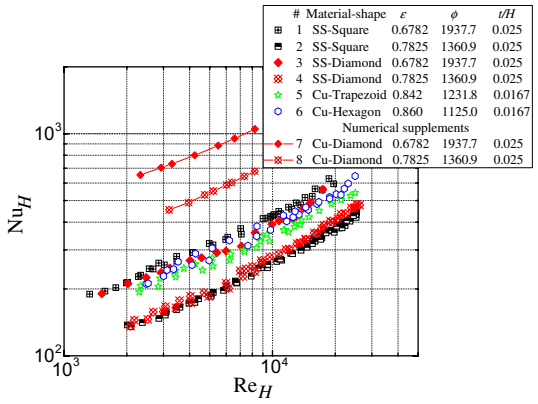

Fig. 7. Nusselt numbers Nu_H of six test samples plotted as functions of Reynolds number Re_H.

The heat dissipation from the heat source to the flowing coolant via the metal honeycomb structure is a combined conduction–convection process. The convection process is highly related to the flow field in honeycomb structure; therefore, two factors (*surface area density* ϕ and *cell shape*) that influence the flow field (discussed above in Section 5.2) are also important when discussing the heat transfer. For the conduction process, two more factors: the *ratio* t/H and the solid material's *thermal conductivity* k_s, need to be taken into consideration.

For the four samples made of stainless steel material (samples 1–4), square- and diamond-shaped honeycomb structures with the same values of ϕ and t/H (sample 1 vs. sample 3, sample 2 vs. sample 4) have the same Nu_H distributions. This once again indicates that the cross-sectional direction have little effect on Nu_H for low Grashof numbers. The higher surface area densities of samples 1 and 3 enable them to transfer more heat than samples 2 and 4.

For samples 5 and 6 made of copper having the same ratio t/H, the Nusselt number for hexagon-shaped sample 6 is slightly higher than that for trapezoid-shaped sample 5, although the surface area density of sample 5 is higher than that of sample 6. Again, this can be attributed to the larger shape number of the hexagon shape than that of the trapezoid shape.

Comparing the Nu_H curves of samples 5–8 made of copper, it is found that the two diamond-shaped samples (7 and 8) have much higher Nu_H values than those of trapezoid- and hexagon-shaped samples (5 and 6). The higher surface area densities of samples 7 and 8 are undoubtedly one reason; and another reason is their higher t/H values, which reduce the thermal conductive resistance in cell wall.

The effect of solid thermal conductivity on the heat transfer rate of 2D cellular metals can be ascertained by comparing the Nu_H curves of samples 3 and 7 as well as samples 4 and 8 (see Fig. 7): the higher the wall conductivity, the higher the heat transfer rate.

5.4. Overall thermal performance

The overall thermal performance can be thought of as the amount of heat Q dissipated from a heat source that is transferred to a heat sink and then to a forced coolant flowing through it with certain inlet temperature $T_{f,in}$. For heat sink design, the ultimate aims include:

(1) The highest temperature in the heat sink, $T_{w,max}$, which occurs at the outlet on the face-sheet attached to the heat source, should be as low as possible.
(2) The imposed pumping power P to obtain the above goal is also hoped to be as low as possible.

In view of this, Valdevit et al. [22] combined the four parameters: Q, P, $T_{f,in}$, $T_{w,max}$, and defined a new objective function $Q/[(T_{w,max} - T_{f,in})P]$ to evaluate the overall thermal performance for different structured heat sinks. Starting from this function, they deduced two indices (Π_h, Π_p)

$$\frac{Q}{T_{w,max} - T_{f,in}} = k_f W \Pi_h \tag{13}$$

and

$$P = \frac{1}{2}\frac{\mu_f^3}{\rho_f^3}\frac{W}{L^2}\Pi_P \tag{14}$$

where

$$\Pi_h = \frac{Nu_H}{(H/L)\left[1 + \frac{Nu_H}{PrRe_H(H/L)}\right]} \tag{15}$$

and

$$\Pi_P = \frac{f_H Re_H^3}{(H/L)^3} \tag{16}$$

While the maps of $Q/(T_{w,max} - T_{f,in})$ against P permits the overall thermal performance comparison for different heat sinks, the maps of Π_h against Π_P give the comparison of overall thermal performance for different heat sinks with the same working fluid.

In the present study, the above indices were first used to rank the overall performance of the six test samples and then compared with other heat sink media.

Comparisons of the six samples are presented in Fig. 8; all data shown are experimentally measured. The hexagon-shaped copper sample 6, despite of its lowest surface area density and t/H ratio, ranks first for its high wall conductivity and the advantages of the hexagon shape; similar results have previously been obtained by Gu et al. [12] using theoretical analysis. Although the trapezoid-shaped copper sample 5 has smaller surface area density and t/H ratio than the other four stainless steel samples, it ranks higher due to its higher wall thermal conductivity. Samples 1 and 3, when compared with samples 2 and 4, are superior due to their higher area surface densities.

Comparisons between the overall thermal performances of metal honeycomb structures and selected heat sink media, including metal foams [23–29], lattice-frame materials [30–33], Kagome structures [34], and woven textile structures [35,36], are presented in Fig. 9. It is shown that for the same expense of the pumping power, the thermal performances of metal honeycomb structures are obviously superior to other heat sink media; or, equivalently, to

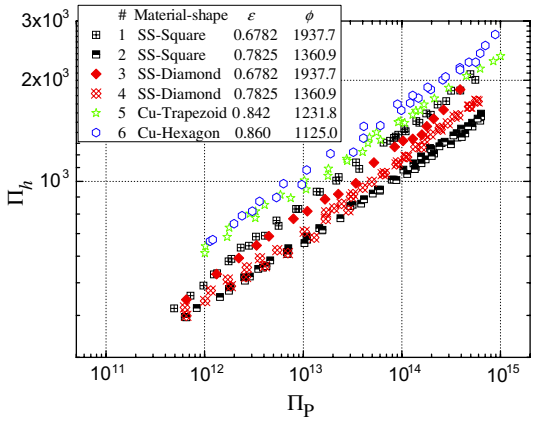

Fig. 8. Map of Π_h against Π_P for overall thermal performance comparison.

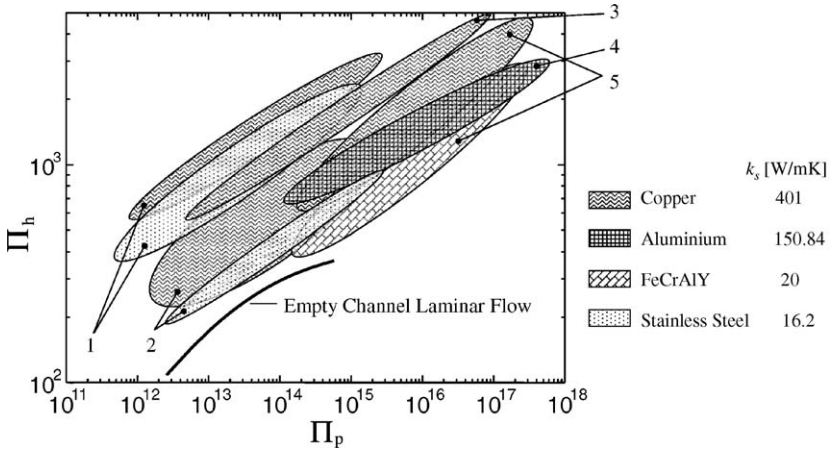

Fig. 9. Map of Π_h against Π_P for metallic honeycomb structures and other heat sink media. 1. Metallic honeycomb structure; 2. Woven textiles [35,36]; 3. Kagome structure [34]; 4. Lattice-frame material [30–33]; 5. Metal foam [23–29].

obtain the same thermal performance, the metal honeycomb structures expense the least friction-power.

6. Conclusions

The performance of sandwiched metallic honeycomb structures with one face-sheet heated by a constant heat flux was experimentally and numerically investigated under forced air convection conditions. Honeycomb structures made of different materials and having different topologies were fabricated and tested. The main conclusions include:

(1) The pressure drop in honeycomb structures mainly depends on two geometric properties: surface area density and cell shape, the effect of latter can be characterized by a dimensionless shape number. Large surface area densities correspond to large friction factors whilst shapes with larger shape numbers cause high pressure drops.
(2) The rate of heat transfer in a honeycomb structure depends not only on geometric properties (surface area density, cell shape and ratio t/H) but also on the thermal conductivity of the wall material. The heat transfer rate of metal honeycomb structures increases with the increase of surface area density or shape number or t/H, while keeping the other two unchanged. A higher thermal conductivity of the wall material can also contribute to heat transfer enhancement.
(3) The overall thermal performance of metal honeycomb structures, as characterized by two dimensionless indices, Π_P and Π_h, are superior to other heat sink media such as metal foams, lattice-frame materials, Kagome structures and woven textile structures.

Acknowledgements

The authors thank the National Basic Research Program of China (Grant No. 2006CB601202), the National 111 Project of China (Grant No. B06024), the National Natural Science Foundation of China (Grant Nos. 10328203 and 10572111), and the EU HYMM project for partial financial support of this work.

References

[1] A.G. Evans, J.W. Hutchinson, N.A. Fleck, M.F. Ashby, H.N.G. Wadley, The topological design of multifunctional cellular materials, Prog. Mater. Sci. 46 (2001) 309–327.
[2] T.J. Lu, H.A. Stone, M.F. Ashby, Heat transfer in open-cell metal foams, Acta Mater. 46 (1998) 3619–3635.
[3] M.F. Ashby, T.J. Lu, Metal foams: a survey, Sci. China (B) 46 (2003) 521–532.
[4] T.J. Lu, F. Chen, D.P. He, Sound absorption of cellular metals with semi-open cells, J. Acoust. Soc. Am. 108 (2000) 1697–1709.
[5] C. Chen, T.J. Lu, N.A. Fleck, Effect of imperfections on the yielding of two-dimensional foams, J. Mech. Phys. Solids 47 (1999) 2235–2272.
[6] J.S. Liu, T.J. Lu, Multi-objective and multi-loading optimization of ultralightweight truss materials, Int. J. Solids Struct. 41 (2004) 619–635.
[7] D. Sypeck, H. Wadley, Multifunctional microtruss laminates: textile synthesis and properties, J. Mater. Res. 16 (2001) 890–897.
[8] I.D.J. Dupere, T.J. Lu, A.P. Dowling, Acoustic properties of cellular solids, in: Paolo Colombo, Michael Scheffler (Eds.), Cellular Ceramics: Structure Manufacturing Properties and Applications, Wiley-VCH, Weinheim, 2004.
[9] T.J. Lu, J.W. Hutchinson, A.G. Evans, Optimal design of a flexural actuator, J. Mech. Phys. Solids 49 (2001) 2071–2093.
[10] L.H. Han, T.J. Lu, A.G. Evans, Minimum weight design of a high authority flexural actuator with electroelastomers, Smart Mater. Struct. 13 (2004) 1211–1221.
[11] T.J. Lu, Heat transfer efficiency of metal honeycombs, Int. J. Heat Mass Transfer 42 (1999) 2031–2040.
[12] S. Gu, T.J. Lu, A. Evans, On the design of two-dimensional cellular metals for combined heat dissipation and structural load capacity, Int. J. Heat Mass Transfer 44 (2001) 2163–2175.
[13] R.S. Kumar, D.L. McDowell, Rapid preliminary design of rectangular linear cellular alloys for maximum heat transfer, AIAA 42 (2004) 1652–1661.
[14] C. Seepersad, B. Dempsey, J. Allen, F. Mistree, D. McDowell, Design of multifunctional honeycomb materials, AIAA 42 (2004) 1025–1033.
[15] A.M. Hayes, A. Wang, B. M Dempsey, D.L. McDowell, Mechanics of linear cellular alloys, in: Proceedings of IMECE 2001, International Mechanical Engineering Congress and Exposition, American Society of Mechanical Engineers, New York, 2001.
[16] B.M. Dempsey, S. Eisele, D.L. McDowell, Heat sink applications of extruded metal honeycombs, Int. J. Heat Mass Transfer 48 (2005) 527–535.
[17] H.W. Coleman, W.G. Steele, Experimentation and Uncertainty Analysis for Engineers, second ed., Wiley, 1999.
[18] FLUENT User's Guide, ver.6.0, Fluent Inc., 1998.
[19] A.P. Colburn, A method of correlating forced convection heat transfer data and a comparison with fluid friction, Int. J. Heat Mass Transfer 7 (1964) 1359–1384.
[20] F.M. White, Fluid Mechanics, third ed., McGraw-Hill, 1994.
[21] A. Bejan, Convection Heat Transfer, second ed., Wiley, New York, 1995.
[22] L. Valdevit, A. Pantano, H.A. stone, A.G. Evans, Optimal active cooling performance of metallic sandwich panels with prismatic cores, International Journal of Heat and Mass Transfer, accepted for publication.
[23] C.Y. Zhao, Thermal Transport in Cellular Metal Foams with Open Cells, Ph.D. Thesis, Department of Engineering, University of Cambridge, 2003.
[24] C.Y. Zhao, T. Kim, T.J. Lu, H.P. Hodson, Thermal transport in high porosity cellular metal foams, J. Thermofluid Phys. 18 (2004) 901–911.
[25] C.Y. Zhao, T.J. Lu, H.P. Hodson, J.D. Jackson, The temperature dependence of effective thermal conductivity of open-celled steel alloy foams, Mater. Sci. Eng. A 367 (2004) 123–131.
[26] K. Boomsma, D. Poulikakos, On the effective thermal conductivity of a three-dimensionally structures fluid-saturated metal foam, Int. J. Heat Mass Transfer 44 (2001) 827–836.
[27] A. Bhattacharya, V.V. Calmidi, R.L. Mahajan, Thermophysical properties of high porosity metal foams, Int. J. Heat Mass Transfer 45 (2002) 1017–1031.
[28] M.S. Phanikumar, R.L. Mahajan, Non-Darcy natural convection in high porosity metal foams, Int. J. Heat Mass Transfer 45 (2002) 3781–3793.
[29] R. Singh, H.S. Kasana, Computational aspects of effective thermal conductivity of highly porous metal foams, Appl. Therm. Eng. 24 (2004) 1841–1849.
[30] T. Kim, Fluid-flow and heat-transfer in a lattice-frame material, Ph.D. Thesis, Department of Engineering, University of Cambridge, 2003.

[31] T. Kim, C.Y. Zhao, T.J. Lu, H.P. Hodson, Convective heat dissipation with lattice-frame materials, Mech. Mater. 36 (2004) 767–780.

[32] T. Kim, H.P. Hodson, T.J. Lu, Fluid flow and endwall heat-transfer characteristics of lattice-frame materials, Int. J. Heat Mass Transfer 47 (2004) 1129–1140.

[33] T. Kim, H.P. Hodson, T.J. Lu, Contribution of vortex structures and flow separation to local and overall pressure and heat transfer characteristics in an ultralightweight lattice material, Int. J. Heat Mass Transfer 48 (2005) 4243–4246.

[34] F. Hoffmann, Heat transfer performance and pressure drop of Kagome core metal truss panels, M.Phil. Thesis, Department of Engineering, University of Cambridge, 2002.

[35] J. Tian, T. Kim, T.J. Lu, H.P. Hodson, D.T. Queheillalt, H.N.G. Wadley, The effects of topology upon fluid-flow and heat-transfer within cellular copper structures, Int. J. of Heat Mass Transfer 47 (2004) 3171–3186.

[36] J. Tian, Fluid flow and heat transfer in woven textiles, Ph.D. Thesis, Department of Engineering, University of Cambridge, 2005.